PAPER

ZnO nanoflowers with single crystal structure towards enhanced gas sensing and photocatalysis

Sha Zhang,[a] Hsueh-Shih Chen,[b] Katarzyna Matras-Postolek[c] and Ping Yang*[a]

In this paper, ZnO nanoflowers (NFs) were fabricated by thermal decomposition in an organic solvent and their application in gas sensors and photocatalysis was investigated. These single crystal ZnO NFs, which were observed for the first time, with an average size of ∼60 nm and were grown along the {100} facet. It was suggested that oleylamine used in the synthesis inhibited the growth and agglomeration of ZnO through the coordination of the oleylamine N atoms. The NFs exhibited excellent selectivity to acetone with a concentration of 25 ppm at 300 °C because they had a high specific surface area that provided more active sites and the surface adsorbed oxygen species for interaction with acetone. In addition, the ZnO NFs showed enhanced gas sensing response which was also ascribed to abundant oxygen vacancies at the junctions between petals of the NFs. Furthermore, ZnO–reduced graphene oxide (RGO) composites were fabricated by loading the ZnO NFs on the surface of the stratiform RGO sheet. In the photodegradation of rhodamine B tests, the composite revealed an enhanced photocatalytic performance compared with ZnO NFs under UV light irradiation.

Introduction

In the past few decades, effectively controlling the size, morphology, and structure of nanoparticles (NPs) has been a hot topic for the development of nanoscience and technology, especially for their applications with morphology-dependent properties.[1] The crystal growth mechanism and the microstructure development at a nanoscale play a critical role in controlling the size-dependent properties.[2–4] Normally, the kinetic model for coarsening of bulk materials is based on the Ostwald ripening mechanism, which involves the dissolution–precipitation processes between particles. Other growth modes may be involved in the growth of NPs. For example, a growth mechanism named "oriented attachment", where two crystallographically oriented NPs combined together to form a larger one, was proved to be another significant mode for nanocrystal growth.[1] The thermal decomposition of precursors in organic solvents containing surfactants at high temperature provides better control over size, shape, composition, and internal structure of the NPs with respect to other methods, such as coprecipitation. To investigate the growth process, much effort has been devoted to the development of NPs with various regular morphologies such as spheres,

sheets, and rods. NPs with other irregular morphologies were also created to study the crystal growth and morphology evolution processes and the corresponding mechanisms. For example, two-dimensional CuO nanoleaves were reported.[1] However, there still exist difficulties and problems in controlling the growth of irregular NPs.

Due to its hexagonal wurtzite structure and polar crystal surfaces, ZnO has diversified nanostructures. Many research groups have developed various synthetic methods to fabricate such nanostructures. Although the solvothermal synthesis has the disadvantages of lower efficiency, environmental pollution, and poor controllability, it was widely applied because of its advantages, such as simple operation and mild reaction conditions. For example, Qiu and co-workers reported on the synthesis of hierarchical ZnO nanorod and nanosheet structures for dye-sensitized solar cells.[5] Kang *et al.* reported the fabrication of hierarchical ZnO nanostructures *via* a surfactant-directed process.[6] The synthesis of ZnO and zinc hydroxide single nanosheets was carried out by delamination of layered ZnO film intercalated with dodecyl sulfate ions which was synthesized by the cathodic electrodeposition process.[7] However, the relationships between the morphology, crystal growth habit, and photocatalytic properties of ZnO single crystal nanoflowers (NFs) have not been elucidated. There is almost no report on the photocatalytic activities of such ZnO NFs.

ZnO is one of the most promising materials for gas sensing application due to its high mobility of conduction electrons and ideal chemical and thermal stability under the operating conditions of sensors.[8,9] In addition, ZnO nanomaterials have

[a] School of Material Science and Engineering, University of Jinan, Jinan, 250022, P. R. China. E-mail: mse_yangp@ujn.edu.cn

[b] Department of Materials Science and Engineering, National Tsing Hua University, Hsinchu 300, Taiwan

[c] Faculty of Chemical Engineering and Technology, Cracow University of Technology, Krakow, 31-155, Poland

been investigated for photocatalytic degradation of pollutants and hydrogen generation from water splitting because of their high catalytic activity, low cost and environmental friendliness.[10–12] Most of them suffer from a wide bandgap, photocorrosion, and low separation efficiency of electron–hole pairs. Because a reaction occurs at the interface between the catalyst surfaces and organic pollutants, the morphologies affecting surface atomic arrangements and coordination play an important role in determining catalytic performance.[13] The morphology and surface atomic structure of exposed facets of ZnO materials affect strongly their properties. Property improvement has also been observed for the composites of ZnO nanomaterials with other materials such as the composite of ZnO nanorods and graphene (GR). The ZnO based composite has become a hot topic.

In this paper, we synthesized flat single crystal ZnO NFs via a thermal decomposition route by adjusting the preparation parameters such as chemical concentration, temperature, and stirring rate. These synthesized single crystalline ZnO NFs with average size $\sim$60 nm, which were observed for the first time, were grown along the {100} facet. Their application in gas sensors and photocatalysis was investigated. ZnO–reduced graphene oxide (RGO) composites exhibited enhanced photocatalytic performance in the degradation of rhodamine B (RhB) under UV light irradiation compared with ZnO NFs.

Experimental

Chemicals

1-Octanol, zinc acetate dehydrate ($Zn(Ac)_2 \cdot 2H_2O$), ethanol, oleylamine, graphite powder, potassium permanganate ($KMnO_4$), sulfuric acid (H_2SO_4), hydrogen peroxide (30%), phosphoric acid (H_3PO_4), hydrochloric acid, and hexane were supplied by Shanghai Chemical Reagent Company and Tianjin Chemical Reagent Company. The commercially available reagents were used without further purification. Deionized water used in the synthesis was obtained from a Milli-Q synthesis system (resistivity $\sim$18 MΩ cm).

Synthesis of ZnO NFs

The typical synthetic process of ZnO NFs is as follows: 0.5 mmol of $Zn(Ac)_2 \cdot 2H_2O$ and 6 mL of 1-octanol were added into a four-neck flask with stirring. Then, 4 mL of oleylamine was added under continued agitation to the mixture of zinc acetate dehydrate and 1-octanol. The mixture was slowly heated to 120 °C and kept at this temperature for 1 h to remove water. After that, the mixture was heat-treated at 180 °C for 30 min with stirring and N_2 purging. After cooling down to room temperature, the products were collected by centrifugation and then washed with equal volumes of ethanol and hexane. Finally, the products were re-dispersed in hexane. The preparation conditions of samples are listed in Table 1.

Synthesis of graphene oxide

Graphene oxide was obtained from natural graphite powder via modified Hummers' method, as reported by Marcano et al.[14] In brief, graphite flakes of 3.0 g were added to a mixture of H_2SO_4

Table 1 Preparation conditions of samples

Sample	Stirring speed (rpm)	Reaction time (min)
1	N/A	30
2	50	30
3	200	30
4	400	30
5	800	30
6	200	5
7	200	10
8	200	15
9	200	30
10	200	60
11	200	90
12	200	35

of 360 mL, H_3PO_4 of 40 mL, and $KMnO_4$ of 18.0 g in a water bath at 50 °C with vigorous stirring. After stirring for 12 h, 400 mL of water with 30% H_2O_2 was added, and a brilliant yellow product was formed with bubbling. The mixture was filtered through polyester fiber and then the supernatant was centrifuged (4000 rpm for 2 h). The remaining sediment was purified in succession by 200 mL of water, 200 mL of 30% HCl, and 200 mL of ethanol for three times. The final sediment was exfoliated in water by an ultrasonic cleaner, giving a solution of graphene oxide.

Synthesis of ZnO–RGO nanocomposites

2.5 mL of ethanol solution containing an appropriate amount of graphene oxide was added into the reacting solution of ZnO NFs under the same experimental conditions. In this process, graphene oxide was reduced to RGO by oleylamine. Finally, ZnO–RGO nanocomposites were obtained.

Photocatalytic measurement

For the photocatalytic degradation of RhB, 0.01 g of catalyst (ZnO NFs or ZnO–RGO nanocomposites) was suspended in 20 mL of RhB dye aqueous solution (10 mg L^{-1}). The mixture was continuously stirred in the dark for 60 min to attain sufficient adsorption on the catalyst surface. Then, the photocatalytic test was carried out using a 20 W UV lamp. 2 mL of the sample was taken out at certain time intervals and centrifuged for the absorbance measurement using a Hitachi U-4100 spectrophotometer.

Characterization

The X-ray powder diffraction (XRD) patterns of ZnO NFs were characterized using a Bruker D8-Advance diffractometer (Bruker, Germany) with a Cu-K$_\alpha$ radiation source. High-resolution transmission electron microscopy (HRTEM) images were obtained using a Philips Tecnai 20U-Twin high-resolution transmission electron microscope at an accelerating voltage of 200 kV. Transmission electron microscopy (TEM) images were obtained using a JEM-2010 electron microscope at an accelerating voltage of 200 kV. The Fourier transform infrared (FT-IR) spectrum was recorded on a Bruker Tensor27 FT-IR spectrometer using KBr pellets. The UV-vis absorption spectra were detected using a Hitachi U-4100 spectrophotometer. The specific surface area of ZnO NFs was measured by using a multi-function adsorption instrument (MFA-140 of Beijing Builder Company).

Before measurement, the ZnO NFs were degassed under vacuum at 110 °C for 2 h.

Results and discussion

Phase composition and morphology of ZnO NFs

ZnO NFs were fabricated through the thermal decomposition of zinc acetate in an organic solvent at 180 °C. A typical XRD pattern of as-synthesized ZnO NFs is shown in Fig. 1. The result indicates that all the XRD peaks could be indexed to the (100), (002), (101), (102), (110), (103), (200), (112), and (201) planes of hexagonal structured ZnO. The XRD patterns of the ZnO crystalline phase with flat self-assembled NFs exhibit well-defined peaks that could be assigned to the wurtzite phase without any impurity. The XRD peaks with high intensity indicate ZnO NFs with high crystallinity.

Fig. 2 shows the typical TEM images of as-synthesized ZnO NFs. The result indicates that the irregular ZnO NFs consist of flat NPs as "building blocks" to attach with each other as shown in Fig. 2a. As far as we know, the ZnO NFs built up from primary ZnO units by sharing the same surfaces or edges were reported for the first time. The high degree of crystallinity of samples was confirmed by HRTEM observations. The detailed structure of an individual ZnO NF is shown in Fig. 2b, which shows that the NPs assembled into a single crystal by sharing identical lattices to form a ZnO NF. A similar phenomenon was observed for the oriented assembly of Fe_3O_4 NPs into monodispersed hollow single-crystal microspheres reported by Yu et al.[15] The well-developed lattice fringes of the NF possess interplane distances estimated to be 0.28 nm (Fig. 2b),
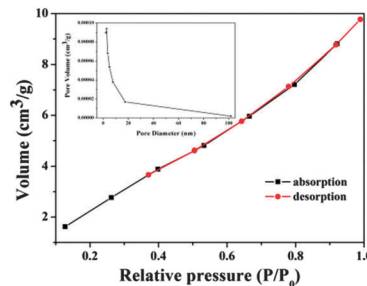
Fig. 3 N_2 adsorption–desorption isotherm and the corresponding pore size distribution of sample 9 in Table 1.

corresponding to the d-spacing of {100} planes of wurtzite ZnO. The surface profiles of the crystalline ZnO NPs reveal that they are mainly composed of the {100} plane, whereas the Zn-rich face of the hexagonal crystalline ZnO NFs is the (001) plane, and the opposite face is the (00$\bar{1}$) plane. The corresponding fast Fourier transform (FFT) pattern from the [001] zone axis of the individual ZnO NF shown in Fig. 2c demonstrates the single-crystalline nature of the individual ZnO NF and the surface of the ZnO NFs mainly composed of {100} planes.[16] In addition, the morphological properties of ZnO NFs depend strongly on stirring rates during preparation. 200 rpm is found to be an optimal value to fabricate the NFs composed of small NPs. The specific surface area and pore-size distribution curve of ZnO NF samples are shown in Fig. 3. ZnO NFs prepared in our experiment had a high specific surface area (12.89 m^2 g^{-1}) in comparison to flower-like ZnO reported in the previous literature.[17,18]

Assembled growth mechanism

To indicate the growth process of ZnO NFs, samples 6–11 were prepared using different reaction times. Because of the reaction between zinc acetate and oleylamine, the formation of ZnO NFs included four steps: (I) aminolytic reaction between zinc acetate and oleylamine, (II) zinc hydroxide decomposition, (III) nucleation, and (IV) growth. When the reaction temperature reaches 180 °C, zinc acetate is converted to zinc hydroxide intermediates by aminolytic reaction as indicated in Scheme 1.[19,20] Then, zinc hydroxide forms ZnO rapidly. Fig. 4 shows the TEM images of samples 6–11 prepared with different reaction times. At the early stage, e.g., 5 min, monodispersed ZnO NPs are generated as shown in Fig. 4a. The diameter of NPs is about 5–10 nm. After 10 min, the NPs develop into small NFs as shown in Fig. 4b. A significant growth occurs when the reaction time is 30 min, which is confirmed by the TEM images shown in Fig. 4d. It should be noted that the NFs obtained at 30 min consist of NPs with a diameter of 10–20 nm. For a longer growth time, i.e., 60 min, the diameter of the NPs increases to 20–35 nm
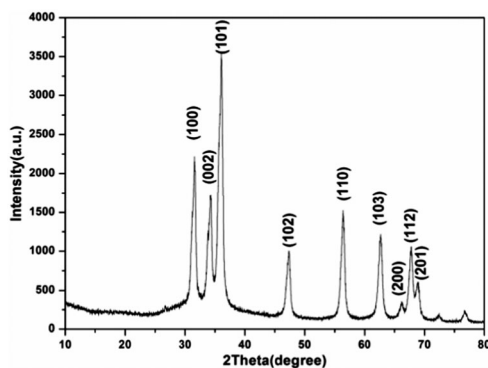
Fig. 1   XRD pattern of as-prepared ZnO NFs (sample 9 in Table 1).
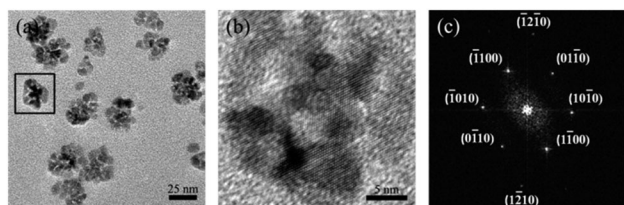
Fig. 2   (a) TEM image of as-prepared ZnO NFs (sample 3 in Table 1). (b) HRTEM image of a selected area shown by the black square in (a). (c) FFT pattern viewed along the [0001] direction of an individual particle shown in (b).
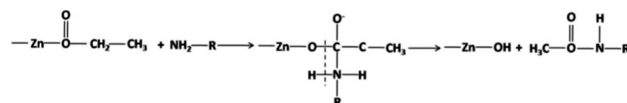
Scheme 1   Aminolytic reaction between zinc acetate and oleylamine.
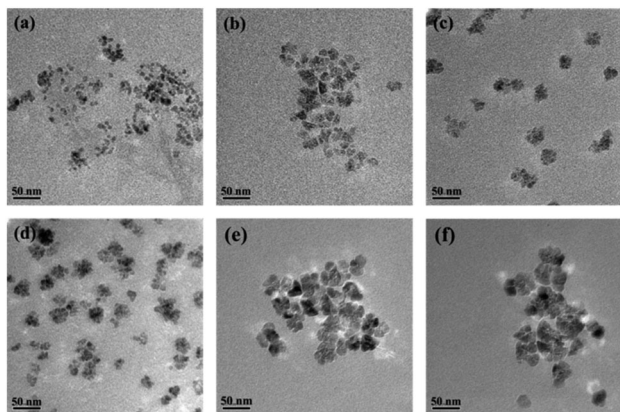

Fig. 4 TEM images of ZnO NFs (samples 6–11 in Table 1) prepared in different reaction times. (a) Sample 6 (5 min), (b) sample 7 (10 min), (c) sample 8 (15 min), (d) sample 9 (30 min), (e) sample 10 (60 min) and (f) sample 11 (90 min).

as shown in Fig. 4e. When the reaction time was prolonged to 90 min, the size and morphology were roughly the same as shown in Fig. 4f.

In order to study the growth mechanism of ZnO NFs, ZnO NF samples were fabricated using a reaction time of 35 min. Fig. 5 shows the TEM images of this sample. These ZnO NFs consisted of small ZnO NPs with a size of 4–12 nm as shown in Fig. 5a and b. The average size of ZnO NFs is about 38 nm. The TEM images in Fig. 5b show that the ZnO NF consisted of small ZnO NPs with an average size of 8 nm. These NPs share an identical crystallographic orientation[21] identified to be the {100} face ($d = 0.28$ nm). The lattice fringes of the (100) plane are clearly observed and have an inter-planar spacing of 0.28 nm, which can be well indexed to the hexagonal ZnO crystal structure. The results confirm that ZnO NFs grow along the (100) direction.
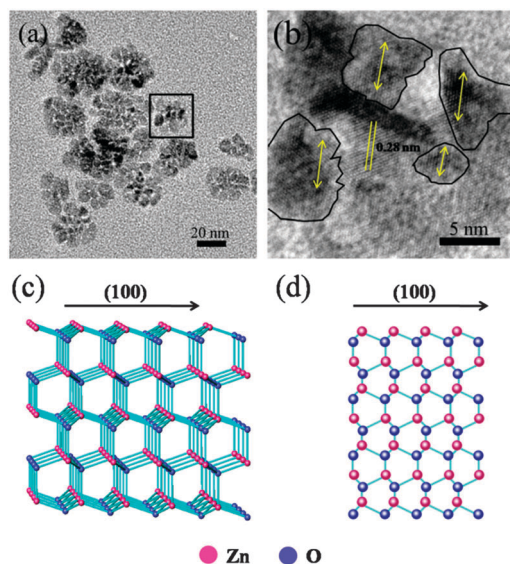

Fig. 5 (a) TEM image of ZnO NFs (sample 12 in Table 1). (b) TEM image of ZnO NF shown as a black square region in (a). (c) Proposed 3D model of ZnO NFs. (d) Proposed 2D model of ZnO NFs.
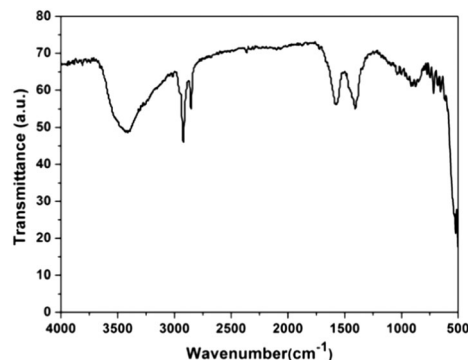

Fig. 6 FTIR spectrum of ZnO NFs (sample 12 in Table 1).

Fig. 5c shows the 3D model of ZnO NFs and Fig. 5d indicates the 2D model of ZnO NFs.

In the formation of ZnO NFs, oleylamine not only acts as a reactant to react with zinc acetate but also acts as an inhibitor to inhibit the growth and agglomeration through the coordination of its N atoms with the surface of metal oxides.[21–23] Fig. 6 depicts a typical FTIR spectrum of the ZnO NFs. The characteristic broad C=O stretching vibrations at 1500–1750 cm^{-1} and the sharp peak at 2800–3000 cm^{-1} indicate that oleylamine molecules were attached to the surface of ZnO NFs tightly.

Gas sensing property

ZnO nanostructures with various morphologies usually show remarkable gas sensing properties because of their high surface area and the fabricated junctions between NPs.[24] For example, nest-like ZnO with hierarchical porous structures has a high response to ethanol and acetone,[25] and ZnO nanowires composed of NPs have an enhanced response to NO$_2$ gas.[26] In the current study, the sensitivity of ZnO NFs toward acetone gas was investigated. Acetone is one of the chemical hazards and toxic substances to our health. The detection of acetone is of great significance for environmental protection and human health. The sensor response of the samples is defined as R_a/R_g, where R_a and R_g are the electrical resistances of the sensor in dry air and in the target gas, respectively. Fig. 7a shows the response of the as-fabricated gas sensor to 100 ppm acetone at working temperatures from 200 to 360 °C.

It is well-known that the response of semiconductor based gas sensors is determined by the chemical reactions between the surface adsorbed oxygen species and acetone gas molecules on the surface of ZnO. At low temperature, the energy is not high enough to support the reaction between acetone gas molecules and the surface-adsorbed oxygen species. Therefore, the response value is relatively low. With increasing temperature, the energy becomes high enough to support the acetone molecules to react with surface-adsorbed oxygen species and therefore the response increases significantly. When the temperature increases to a certain value, the R_a/R_g exhibits the highest value. After that, the response value of the gas sensor decreases because of the difficulty in acetone gas adsorption.[27,28] For ZnO NF sensors, the response first increases abruptly with the working temperature and then gradually decreases. The best working temperature
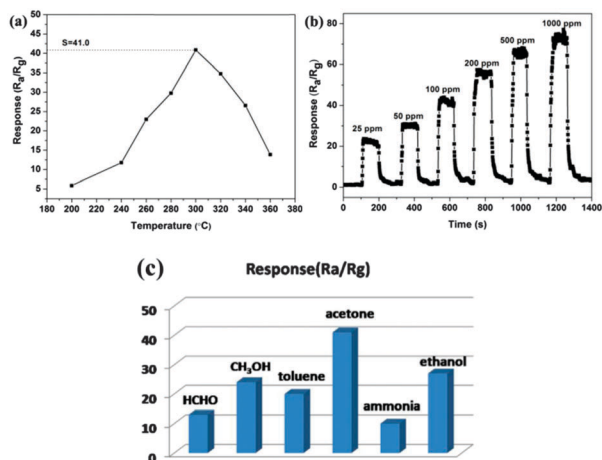

Fig. 7 (a) Gas sensing response values of the as-fabricated gas sensor with different working temperatures in 100 ppm acetone. (b) Time–response curve of the ZnO NFs (sample 9 in Table 1) as sensors to acetone working at 300 °C. (c) Responses of sensors based on ZnO NFs to various gases (100 ppm).

found in the current study is 300 °C, while the corresponding response to acetone is 41.0. Fig. 7b shows the real-time sensor response curves of the ZnO NF sensor to acetone with different concentrations at an optimal working temperature of 300 °C. It clearly shows that the response values increase with increasing gas concentration from 25 to 1000 ppm. The response and recovery times, as important parameters for evaluating the properties of gas sensors, are also investigated. It has to be noted that the response and recovery times are calculated as 21 and 9 s at the gas concentration of 100 ppm, respectively, showing the great properties of the ZnO NF sensor. Moreover, the sensor is found to be stable after operating for 5 cycles, which indicates that this sensor has vital applications in detecting acetone gas.

Compared with the result reported in the literature,[27] it is obvious that the response of the ZnO NF sensor in our experiment is higher than that of other ZnO nanomaterials toward 100 ppm of acetone. The enhancement in the gas sensing property of ZnO NFs can be explained by the following two reasons. First, a flat ZnO NF is composed of small NPs with a high specific surface area. As demonstrated by HRTEM images, the ZnO NFs have a size between 30 and 60 nm. The ZnO NFs with a high specific surface area provide more active sites for acetone gas molecules, which increases the percentage of surface-adsorbed oxygen species interacting with acetone. Thus, the ZnO NFs have a much better gas sensing response. Second, the enhancement in the gas sensing response can also be attributed to abundant oxygen vacancies that are obtained from the junctions. As shown in Fig. 4c, a lot of junctions between ZnO NPs existed in a single ZnO NF, which possess abundant oxygen vacancies and facilitate the adsorption of active oxygen ions, such as O^{2-}, O^{-}, and O^{2-}.[29] Therefore, the ZnO NF sensor has an excellent acetone sensing property.

Selectivity is another important criterion in gas sensing. Fig. 7c demonstrates the selectivity test of pure ZnO NFs to

various volatile organic compounds, such as HCHO, CH_3OH, toluene, acetone, ammonia, and ethanol. All of the gases were detected at an operating temperature of 300 °C with a concentration of 100 ppm. As shown in Fig. 7c, it is found that ZnO NFs exhibited enhanced response to acetone in comparison to any other gases. The above results confirmed that ZnO NFs had good sensitivity and selectivity to acetone.

Photocatalytic properties of ZnO NFs and ZnO–RGO samples

ZnO, as one of the most promising UV-light driven photocatalysts, has been widely studied for photodegradation of pollutants and conversion of solar to chemical energy. However, the photocatalytic activity of pure ZnO is still poor due to the photocorrosion and low quantum efficiency of ZnO. To solve these problems, many efforts have been made to inhibit the recombination of electron–hole pairs and improve the anti-photocorrosion, such as ZnO–noble metal composites,[30] QD–ZnO composites,[31] and graphite-like carbon–ZnO composites.[32] Among these, constructing ZnO–graphene nanocomposites is a promising method to obtain enhanced photocatalytic performance. The morphology of ZnO–RGO nanocomposites was characterized by TEM as shown in Fig. 8. Clearly, numerous ZnO NFs are densely loaded on the surface of the stratiform RGO sheet, implying that ZnO NFs and the RGO sheet are interfacially contacted with each other closely. Because of the intimate connection between ZnO NFs and RGO sheets, the nanocomposites may potentially offer enhanced electronic interaction. The photocatalytic activity of ZnO NFs and ZnO–RGO composites is evaluated by the degradation of RhB under UV light irradiation. Fig. 9 displays the time-dependent absorption spectra of RhB aqueous solution under UV light irradiation in the presence of the above-mentioned samples and degradation efficiency *versus* reaction time for two samples.

The normalized temporal concentration changes (C/C_0) of RhB during photodegradation are proportional to the normalized maximum absorbance (C/C_0).[33] It is clear that the ZnO–RGO composite shows a remarkable enhancement in the photodegradation of RhB compared with ZnO NFs. Under UV light illumination for 40 min, almost 80% of initial RhB dyes were decomposed by RGO–ZnO. In contrast, ZnO NFs revealed a relatively slow degradation rate for RhB dyes. Thus, ZnO–RGO possesses higher separation efficiency of charge carriers than individual ZnO NFs which is
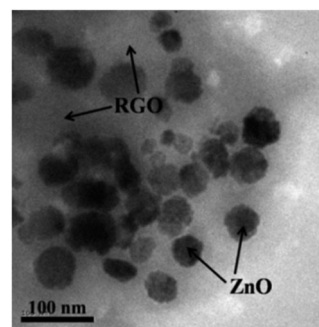

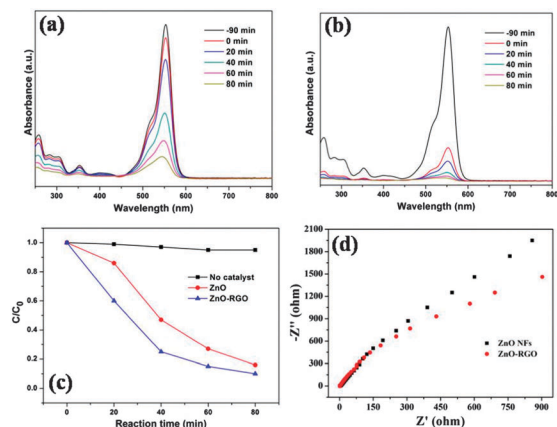Fig. 8 TEM image of the as-prepared ZnO–RGO sample.

Fig. 9 Variation in the adsorption of aqueous RhB under UV light irradiation. (a) With ZnO NFs (sample 9 in Table 1). (b) With ZnO–RGO nanocomposites. (c) Degradation efficiency *versus* reaction time for two samples. (d) EIS Nyquist plots of ZnO NFs ([KOH] = 3 M).

in accordance with the results of the photodegradation of RhB dye. In addition, the pure ZnO NFs possess higher photocatalytic activity than the flower-like ZnO in the reported literature.[34,35]

The typical electrochemical impedance spectrum (EIS) is a useful method to reflect the migration and transfer processes of photogenerated electrons and holes. The radius of the arc in the EIS spectra can indicate the interface layer resistance occurring on the surface of the electrode. The smaller the arc radius, the higher the charge transfer efficiency.[36,37] Fig. 9d shows the Nyquist plots of ZnO NFs and ZnO–RGO composites. Obviously, the arc radius for the ZnO–RGO composite is much smaller than that of the individual ZnO NF, indicating that the ZnO–RGO composite possesses a greater ability for separation and transfer of photogenerated electrons and holes.

Scheme 2 shows the schematic illustration of the charge transfer, enhanced photocurrent, or photocatalytic activity of ZnO–RGO composites. Under UV light illumination, ZnO was excited to form the photogenerated electron–hole pairs, which separated at the interfaces of ZnO NFs and RGO sheets. The photogenerated electrons can react with the adsorbed O_2 to form radicals such as $^{\bullet}O_2{}^{-}$, for the photodegradation of methyl
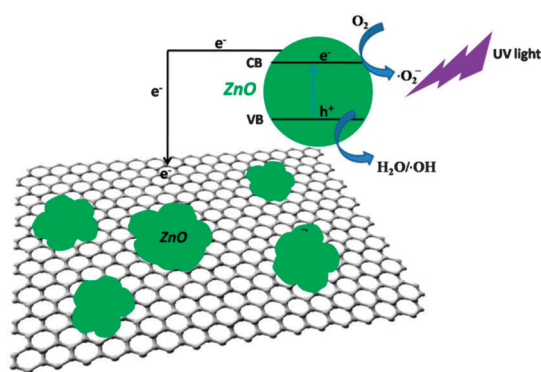
blue, and the remaining holes in ZnO NFs can take part in the redox reactions in the photocatalytic process of RhB dyes.[38] The photogenerated electrons can be transferred from the conduction band of ZnO to RGO, and the RGO serves as an acceptor of electrons and suppresses charge recombination effectively, resulting in higher photocurrent density and more charge carriers to form reactive species, promoting the photodegradation of RhB dyes.[39–42] Therefore, ZnO–RGO composites exhibited enhanced photocatalytic activity.

Conclusions

Thermal decomposition in an organic solvent was developed to synthesize flat ZnO NFs. The applications of these NFs in gas sensors and photocatalysis were investigated. These single crystal ZnO NFs with an average size of 60 nm were grown along the {100} facet. Besides acting as a reaction agent, it was found that oleylamine inhibited the growth and agglomeration possibly through the coordination of its N atoms with the surface of metal oxides. Because the NFs with a high specific surface area provided abundant active sites which increased surface adsorbed oxygen species interacting with acetone, the NFs showed ideal selectivity to acetone with a concentration of 25 ppm at 300 °C. ZnO–RGO composites were fabricated through densely loading the NFs on the surface of the stratiform RGO sheet. Under UV light irradiation, ZnO–RGO composites revealed enhanced photodegradation for RhB. These properties are considered to be important for their applications.

Acknowledgements

Notes and references

1 H. Xu, W. Wang, W. Zhu, L. Zhou and M. Ruan, *Cryst. Growth Des.*, 2007, **7**, 2720.
2 T. Lv, L. K. Pan, X. J. Liu, T. Lu, G. Zhu and Z. Sun, *J. Alloys Compd.*, 2011, **509**, 10086.
3 Y. Yang, L. L. Ren, C. Zhang, S. Huang and T. X. Liu, *ACS Appl. Mater. Interfaces*, 2011, **3**, 2779.
4 Q. Akhavan, *Carbon*, 2011, **49**, 11.
5 J. Qiu, M. Guo and X. Wang, *ACS Appl. Mater. Interfaces*, 2011, **3**, 2358.
6 X. L. Zhang, R. Qiao, R. Qiu, J. C. Kim and Y. S. Kang, *Cryst. Growth Des.*, 2009, **9**, 2907.
7 O. Altuntasoglu, Y. Matsuda, S. Ida and Y. Matsumoto, *Chem. Mater.*, 2010, **22**, 3158.
8 M. Huang, S. Mao, H. Feick, H. Yan, Y. Wu, H. Kind, E. Weber, R. Russo and P. D. Yang, *Science*, 2001, **292**, 1897.

Scheme 2 Proposed mechanism for the enhanced photocurrent density and photocatalytic activity of RGO–ZnO nanocomposites.

This journal is © the Owner Societies 2015

Phys. Chem. Chem. Phys., 2015, **17**, 30300–30306 | **30305**

9 Q. Wan, Q. H. Li, Y. J. Chen, T. H. Wang, X. L. He, J. P. Li and C. L. Lin, *Appl. Phys. Lett.*, 2004, **84**, 3654.

10 L. Liao, H. B. Lu, J. C. Li, H. He, D. F. Wang, D. J. Fu, C. Liu and W. F. Zhang, *J. Phys. Chem. C*, 2007, **111**, 1900.

11 A. Fujishima and K. Honda, *Nature*, 1972, **238**, 37.

12 V. Etacheri, R. Roshan and V. Kumar, *ACS Appl. Mater. Interfaces*, 2012, **4**, 2717.

13 L. Zhang, L. Yin, C. Wang, N. Lun and Y. Qi, *ACS Appl. Mater. Interfaces*, 2010, **2**, 1769.

14 D. C. Marcano, D. V. Kosynkin, J. M. Berlin, A. Sinitskii, Z. Sun, A. Slesarev, L. B. Alemany, W. Lu and J. M. Tour, *ACS Nano*, 2010, **4**, 4806.

15 D. Yu, X. Sun, J. Zou, Z. Wang, F. Wang and K. Tang, *J. Phys. Chem. B*, 2006, **110**, 21667.

16 L. Zhang, L. Yin, C. Wang, N. Lun and Y. Qi, *ACS Appl. Mater. Interfaces*, 2010, **2**, 1769.

17 C. Gu, J. Huang, Y. Wu, M. Zhai, Y. Sun and J. Liu, *J. Alloys Compd.*, 2011, **509**, 4499.

18 S. Ma, J. Xue, Y. Zhou and Z. Zhang, *J. Mater. Chem. A*, 2014, **2**, 7272.

19 O. Karaagac and H. Kockar, *J. Supercond. Novel Magn.*, 2012, **25**, 2777.

20 S. Mourdikoudis and L. M. Liz-Marzán, *Chem. Mater.*, 2013, **25**, 1465.

21 Z. Zhang, H. Sun, X. Shao, D. Li and H. Yu, *Adv. Mater.*, 2005, **17**, 42.

22 M. Green, *Chem. Commun.*, 2005, 3002.

23 Y. Jun, J. Choi and J. Cheon, *Angew. Chem., Int. Ed.*, 2006, **45**, 3414.

24 S. Tian, F. Yang, D. Zeng and C. Xie, *J. Phys. Chem. C*, 2012, **116**, 10586.

25 X. Wang, W. Liu, J. Liu, F. Wang, J. Kong, S. Qiu, C. He and L. Luan, *ACS Appl. Mater. Interfaces*, 2012, **4**, 817.

26 S. Park, S. An, H. Ko, C. Jin and C. Lee, *ACS Appl. Mater. Interfaces*, 2012, **4**, 3650.

27 X. Li, X. Zhou, H. Guo, C. Wang, J. Liu, P. Sun, F. Liu and G. Lu, *ACS Appl. Mater. Interfaces*, 2014, **6**, 18661.

28 G. Neri, A. Bonavita, G. Micali, G. Rizzo, E. Callone and G. Carturan, *Sens. Actuators, B*, 2008, **132**, 224.

29 Y. Zhang, J. Xu, Q. Xiang, H. Li, Q. Pan and P. Xu, *J. Phys. Chem. C*, 2009, **113**, 3430.

30 P. Li, Z. Wei, T. Wu, Q. Peng and Y. Li, *J. Am. Chem. Soc.*, 2011, **133**, 5660.

31 D. Kannaiyan, E. Kim, N. Won, K. W. Kim, Y. H. Jang, M.-A. Cha, D. Y. Ryu, S. Kimc and D. H. Kim, *J. Mater. Chem.*, 2010, **20**, 677.

32 Q.-P. Luo, X.-Y. Yu, B.-X. Lei, H.-Y. Chen, D.-B. Kuang and C.-Y. Su, *J. Phys. Chem. C*, 2012, **116**, 8111.

33 H. Zhang, X. J. Lv, Y. M. Li, Y. Wang and J. H. Li, *ACS Nano*, 2010, **4**, 380.

34 H. Sun, Y. Yu, J. Luo, M. Ahmad and J. Zhu, *CrystEngComm*, 2012, **14**, 8626.

35 M. Ahmad, S. Yingying, A. Nisar, H. Sun, W. Shen, M. Wei and J. Zhu, *J. Mater. Chem.*, 2011, **21**, 7723.

36 Z. Hosseini, N. Taghavinia, N. Sharifi, M. Chavoshi and M. Rahman, *J. Phys. Chem. C*, 2008, **112**, 18686.

37 X. J. Bai, L. Wang, R. L. Zong, Y. H. Lv, Y. Q. Sun and Y. F. Zhu, *Langmuir*, 2013, **29**, 3097.

38 L. C. Jiang and W. D. Zhang, *Electrochim. Acta*, 2010, **56**, 406.

39 C. Y. Kuo, *J. Hazard. Mater.*, 2009, **163**, 239.

40 L. W. Zhang, H. B. Fu and Y. F. Zhu, *Adv. Funct. Mater.*, 2008, **18**, 2180.

41 Q. Liu, Z. Liu, X. Zhang, L. Yang, N. Zhang, G. Pan, S. Yin, Y. Chen and J. Wei, *Adv. Funct. Mater.*, 2009, **19**, 894.

42 X. Wang, L. J. Zhi and K. Mullen, *Nano Lett.*, 2008, **8**, 323.